Tomographic Inversion of the 135.6 nm Emission: The Importance of Radiation Transport in the Nighttime and Terminator Regions

K. F. Dymond[1], A. C. Nicholas[1], S. A. Budzien[1], A. W. Stephan[1], C. Coker[1],
M. A. Hei[2], and K. M. Groves[3]

[1] Space Science Division, Naval Research Laboratory, Washington, DC, USA.

[2] Praxis Inc., Arlington, VA, USA.

[3] Boston College, Institute for Scientific Research, 885 Centre Street, Newton, MA, USA.

Abstract

The 135.6 nm emission of atomic oxygen has become a workhorse for satellite remote sensing of the nighttime ionosphere. Previous work on interpreting the 135.6 nm emission carried out at the Naval Research Laboratory (NRL) and more recent research carried out elsewhere have confirmed the importance of properly modeling the Mutual Neutralization and Radiative Recombination contributions to the volume emission rate and emphasized the importance of modeling and interpreting the transfer and transport of the radiation. Recently, we have developed and published a new inversion approach called Volume Emission Rate Tomography, which handles the radiation transfer as part of the tomography process. We apply the VERT technique to the 135.6 nm measurements made by the Special Sensor Ultraviolet Limb Imager (SSULI) instruments aboard the Defense Meteorological Satellite Program satellites made during ALTAIR overflights in 2010 and 2014. We determine the electron density distribution including all of the effects and sources mentioned above and validate our results against the ALTAIR measurements. We first test the inversion technique against the ALTAIR measurements in 2010, which assesses the technique during nighttime conditions when it should perform most accurately. As the 2014 measurements were made when the terminator was above the northern portion of the ALTAIR field-of-view, we also assess the accuracy of the 1-D plane-parallel, radiation transfer calculations and their effect on the retrieved densities when resonant scattering of dayside emissions into the terminator and nightside is more problematic.

1. Introduction

Previous work at the Naval Research Laboratory [*Dymond et al.,* 1997; *Dymond*, 2009] and in a recent paper published in the Journal of Geophysical Research [*Qin et al.*, 2015] emphasized the importance of radiation transport and radiation transfer when modeling and interpreting the 135.6 nm nightglow. Throughout this work we refer to radiation transport as the redistribution of photons spatially due to multiple resonant scattering and radiation transfer as the process or processes whereby photons are lost from the observer's line-of-sight either by scattering out of the line-of-sight or by absorption of the photons. The *Qin et al.* [2015] paper presents the full tomographic solution of the 135.6 nm nightglow problem to produce ionospheric electron densities and discusses the problems associated with ignoring the mutual neutralization source. The *Dymond et al.* [1997] paper discusses a profile-based (1D) solution approach that used both the 135.6 nm emission and its companion emission at 91.1 nm. As the 91.1 nm emission is produced solely by radiative recombination of O^+ ions and electrons while the 135.6 nm emission is produced by radiative recombination and mutual neutralization and the mutual neutralization source is dependent on the O density, the simultaneous inversion of both emissions can be used to also infer the nighttime O and electron density profiles; however, for the algorithm to infer both profiles, the signal-to-noise ratio of the 91.1 and 135.6 nm emission profiles must be sufficiently high. The 1D model of *Dymond et al.* [1997] has been validated against ionosondes using the Low-Resolution Airglow and Aurora Spectroscopy (LORAAS) instrument data that flew on the *Advanced Research and Global*

Observing Satellite (ARGOS) mission made during overflights of ionosondes in late 1999 [*Dymond et al*., 2001a]. The 91.1 nm emission was found to be too noisy during these validations and thus the 1D inversions used the Mass Spectrometer and Incoherent Scatter (MSIS-86) model [*Hedin*, 1987] for the O and O_2 densities, which are needed to model the mutual neutralization source (O), the multiple resonant scattering (O), and the pure absorption of the photons (O_2). The agreement between the LORAAS measurements and ionosondes was found to be very good, although a very limited set of measurements was presented. Subsequent testing of the 1D 135.6 nm algorithm using Special Sensor Ultraviolet Imager (SSULI) [*McCoy et al.*, 1994; *Dymond et al.,* 2017b] measurements on the *Defense Meteorological Satellite Program* (DMSP) F-18 satellite made during 2010 also showed very good agreement during ionosonde overflights [*Straus*, 2012]; these inversions also ignored the 91.1 nm emission and used the NRLMSISE-00 model [*Picone et al*., 2002] for the O and O_2 densities. *Dymond and Thomas* [2001] presented a tomographic algorithm for analyzing the ionospheric nightglow. This algorithm was developed for the 91.1 nm emission, but worked equally well for the 135.6 nm emission, when the forward model was modified to incorporate the mutual neutralization reaction as well as the radiative recombination reaction. This algorithm did not include radiation transport and radiation transfer effects, but was validated using the Advanced Research Project Agency Long-range Tracking and Identification Radar (ALTAIR) [*Tsunoda et al*., 1979] incoherent scatter radar and found to produce accurate results [*Straus*, 2012]. During 2014-2015, NRL developed new tomography algorithms called Volume Emission Rate Tomography (VERT) based on Image Space Reconstruction techniques [*Dymond, Budzien, and Hei*, 2015; *Dymond, Budzien, and Hei*, 2017]. These algorithms are based on non-negative iteration techniques that permit rapid inversion of UV satellite data. Additionally, the algorithms included the radiation transfer, or the transmission of the radiation, from its source to the observer into the path-length matrix. These algorithms assumed the NRLMSISE-00 [*Picone et al.*, 2002] model for the O and O_2 densities. The VERT technique was validated using SSULI-F19 measurements at 91.1nm made during overflights of the ALTAIR incoherent scatter radar made during 2014 [*Dymond et al*., 2015; *Dymond et al.*, 2017a]. After the volume emission rate is determined by the VERT technique, a physical model of the emission must be inverted to ascertain the electron densities.

The SSULI-F18 overflights of ALTAIR in 2010 occurred at approximately ~20:00 LT, while the SSULI-F19 overflights of ALTAIR in 2014 were made nearer the terminator at ~18:20 LT; these two sets of measurements made with nearly identical instruments and viewing geometries provide a stressing test of the newly developed VERT algorithm and furthermore permit assessments of the practical importance of including the mutual neutralization source in the inversions and of the plane-parallel approximation for the radiation transport of the 135.6 nm emission used in the both the *Dymond et al*. [1997] and *Qin et al*. [2015] algorithms. In this work, we attempt to answer the following questions: 1) How important is the modeling of the Mutual Neutralization source when calculating the electron densities in practical cases? 2) How important is the inclusion of radiation transport in practical cases? 3) If proper modeling of these two sources of emission is included, is it possible to interpret 135.6 nm emission measurements in the region of the solar terminator? 4) Lastly, is 2D radiation transport required in the terminator region? To answer these questions, we compared electron densities derived from ALTAIR measurements to those derived by tomographically inverting the 135.6 nm assuming that the emission is optically thin with no mutual neutralization source and compared the electron densities retrieved using the full-physical model of the 135.6 nm emission, in which radiation transfer, radiation transport, radiative recombination, and mutual neutralization were all included.

This work begins with a short introduction to the SSULI measurements. The physics of the 135.6 nm emission and the inversion approach are then presented. This is followed by a discussion of the comparisons between the SSULI and ALTAIR measurements. Lastly, we present our summary and conclusions.
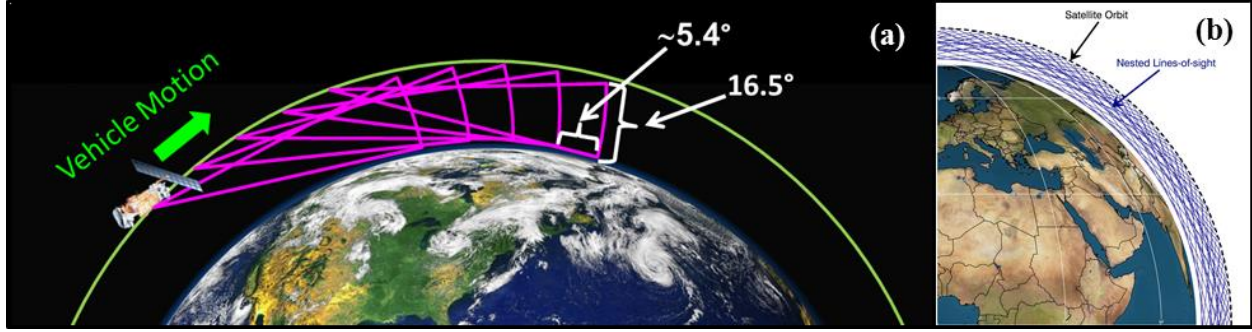
Figure 1: Panel (a) shows a cartoon of the SSULI observing scenario. The sensors view ahead of the DMSP satellites in the orbit plane. A limb scan begins ~26.6° below the satellite's local horizon (tangent height ~100 km) and the scan proceeds upward at a rate of 0.13°·s⁻¹ for the first 60 seconds, then the scan rate increases to 0.28°·s⁻¹ for 30 seconds, until the line-of-sight is ~10° below the satellite's local horizon at a tangent height of ~740 km. Then, a fly-back of the scan occurs sweeping the line-of-sight downward in ~2 seconds, to begin the next scan. This results in a scan every 92 seconds so scans are made at 5.4° spacing along the orbit plane. Panel (b) shows the SSULI lines-of-sight to be nested such that the sensors over-sample the region beneath the vehicle's orbit thereby permitting a tomographic inversion of the measurements to more accurately capture spatial gradients.

2.   SSULI Observations

This work focuses on tomography using the SSULI instruments, limb imagers that view ahead of the DMSP satellites in the orbit plane. Figure 1 shows an example of the how the SSULI instruments sample the atmosphere and ionosphere above the Earth's limb. By aggregating limb scans to take advantage of oversampling imagery in the orbit plane, the lines-of-sight are seen to intersect thereby enabling tomographic interpretation of the measurements. The instruments measure the brightness with ~10 Km altitude resolution at 1 second cadence covering the 750-100 Km altitude range. A limb scan is performed roughly every 92 seconds, depending on the sensor's mode of operation and the fly-back rate of the field-of-view. The SSULI instruments and their measurements are described in detail in *McCoy et al.* [1994] and *Dymond et al.* [2017b].

A SSULI instrument acquires a spectrum covering the 80-170 nm wavelength range at 1.6 nm spectral resolution each second. Each spectrum is de-convolved using a variant of the Richardson-Lucy [*Richardson*, 1972; *Lucy*, 1974] algorithm described in *Dymond, Budzien, and Hei* [2015, 2017] and point spread functions (or line-shapes) that are empirically determined on-orbit. A basis set of 40 spectral features associated with known airglow emissions and instrumental background are used in the deconvolutions. The result of the deconvolution is a set of 40 count rates that can be converted into radiances in units of Rayleighs by division by the instrument's sensitivity at that wavelength. This sensitivity is monitored and tracked on-orbit using serendipitous observations of UV stars measured by other observers during astrophysical observations *Dymond et al*. [2017b].

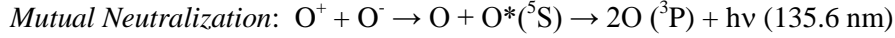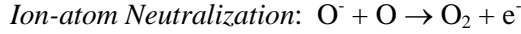## 3.   Physics of the O I 135.6 nm Emission

Emission Photochemistry

The O I 135.6 nm emission is present in both Earth's dayglow and nightglow spectra. It is produced by reactions that are in part responsible for the decay of the ionosphere during daytime and nighttime. But during the daytime, the principal excitation mechanism is photoelectron impact excitation of O and O_2.

The ionospheric reactions are radiative recombination and mutual neutralization. Radiative recombination is the chemical recombination of O^+ ions with electrons resulting in a neutral oxygen atom in an excited electronic state that decays to the ground state with the emission of a photon, *viz*:

$$O^+ + e^- \rightarrow O^*(^5S) \rightarrow O\ (^3P) + h\nu\ (135.6\ nm)$$
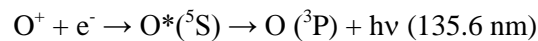
Mutual neutralization is the recombination of O^+ ions and O^- ions. O^- ions are created by radiative attachment of an electron to a neutral oxygen atom. The relevant reactions are:

Radiative Attachment: $O + e^- \rightarrow O^- + h\nu$ (Long wavelength infrared)

Ion-atom Neutralization: $O^- + O \rightarrow O_2 + e^-$

Mutual Neutralization: $O^+ + O^- \rightarrow O + O^*(^5S) \rightarrow 2O\,(^3P) + h\nu$ (135.6 nm)

The volume emission rate, ε_0, for these two reactions is given by:

$$\varepsilon_0(z) = \gamma\,\beta_{1356}\frac{k_1 k_2 n_e(z) n_O(z) n_{O^+}(z)}{k_2 n_{O^+}(z) + k_3 n_O(z)} + \gamma\,\alpha_{1356} n_e(z) n_{O^+}(z) \tag{1}$$

where the first term is the volume emission rate for mutual neutralization and the second term is the volume emission rate for radiative recombination. The reaction rate coefficients ($k_1, k_2,$ and k_3), the radiative recombination rate coefficient (α_{1356}), the production fraction (β_{1356}), and the branching ratio (γ) are all taken from *Melendez-Alvira et al.* [1999] and $n_e, n_O,$ and n_{O^+} are the electron, oxygen, and O^+ densities, respectively. In our analyses below, the O density is taken from the NRLMSISE-00 model [*Picone et al.*, 2002]. In the nighttime F-region ionosphere, the electron and O^+ densities are equal, so that the electron density can be used in place of the O^+ density when calculating the volume emission rate. This expression is used to calculate the initial volume emission rate, ε_0.

Radiation Transport

The photons initially created are redistributed in altitude by multiple resonant scattering with O atoms which redistributes the photons both horizontally and vertically. However, the horizontal O density gradients are much lower than the vertical density gradients so most of the redistribution is vertical and the plane-parallel approximation has been shown to accurately model the transport process. The 135.6 nm emission originates in the ^5S upper state while the ground state of atomic oxygen is the ^3P state causing the transitions between these states to be spin-forbidden. The 135.6 nm emission is a doublet with wavelengths of 135.6 and 135.8 nm. Both lines are resonantly scattered by atomic oxygen and absorbed by molecular oxygen. The resonant scattering redistributes the photons both horizontally and vertically. However, the horizontal density gradients are much lower than the vertical density gradients so most of the redistribution is vertical and the plane-parallel approximation has been shown to accurately model the transport process. The line center scattering cross-sections for the scattering are: 2.499×10^{-18} cm^2 (135.6 nm) and 1.242×10^{-18} cm^2 (135.8 nm) [*Meier*, 1991], and thus the optical depth for the 135.6 nm emission is approximately twice the optical depth of the 135.8 nm emission. Photons are absorbed by molecular oxygen in the Schumann-Runge continuum [*Meier*, 1991]. The absorption cross-sections are: 7.20×10^{-18} cm^2 (135.6 nm) and 7.15×10^{-18} cm^2 (135.8 nm) [*Wang et al.*, 1987]. The scattering optical depth of the 135.6 nm emission integrated from infinity to the altitude where the O density peaks, ~105 km, approaches ~1. This permits the radiation transport to be modeled in the computationally fast Complete Frequency Redistribution Approximation [*Meier*, 1991; *Dymond et al.*, 1997]. Furthermore, when modeling the nighttime radiation transport, the atmosphere can be treated as isothermal with little loss in accuracy.

In this work, the radiation transport is modeled using the integral version of the radiation transport equation in the plane-parallel Complete Frequency Redistribution approximation [*Meier*, 1991; *Dymond et al.*, 1997; *Dymond*, 2009]. The integral equation for the photon transport is:

$$\varepsilon(z) = \varepsilon_0(z) + n_o(z)\sigma \int_{z_{min}}^{z_{max}} \varepsilon(z')H\Big(\big|\tau(z) - \tau(z')\big|, \big|t(z) - t(z')\big|\Big)dz' \tag{2}$$

where z_{max} and z_{min} are the upper and lower limits of the altitude, typically 1000 km and 90 km, respectively, and ε is the volume emission rate. The optical depths for scattering and absorption are:

$$\tau(z) = \sigma \int_z^\infty n_O(z')dz'$$

$$t(z) = \sigma_{O_2}^{abs} \int_z^\infty n_{O_2}(z')dz'$$

The Holstein H function is the probability that a photon originating altitude z′ altitude reaches altitude z integrated over the entire plane perpendicular to z:

$$H(\tau, t) = \frac{1}{2\sqrt{\pi}} \int e^{-2x^2} E_1\Big(\tau e^{-x^2} + t\Big)dx$$

The integration is carried out over all photon frequencies. The function, E_1, is the exponential integral function of the first kind. Equation 2 is a Fredholm integral equation of the first kind. This equation is typically solved by discretization in z and then assuming that the volume emission rate is approximately constant over the z layers and evaluation of the integrals of the Holstein function over the layers. This procedure results in a system of equations that is solved by matrix inversion.

Radiation Transfer

Once the photons are created and then scattered or redistributed in altitude, one needs to model the transfer of that radiation from its source to the observer. The equation for the 135.6 nm brightness is:

$$I_{1356} = 10^{-6} \sum \int_0^\infty T\Big(\big|\tau(z(s)) - \tau^s(z(s=0))\big|, \big|t^s(z(s)) - t^s(z(s=0))\big|\Big)\, \varepsilon(z(s))ds \tag{3}$$

where the summation is carried out over the two lines in the doublet because the SSULI instrument cannot spectrally resolve them. The Holstein transmission function or T-function is defined:

$$T(\tau, t) = \frac{1}{\sqrt{\pi}} \int_{-\infty}^\infty e^{-x^2} \exp(-\tau e^{-x^2} + t)dx$$

where x, denotes the frequency in Doppler units. Equation 3 is another example of a Fredholm integral equation of the first kind. To solve for the volume emission rate in a tomographic sense, the equation is normally discretized into voxels where the volume emission rate is assumed to be constant. Then, the system is solved to infer the volume emission rate. In this work, we assume that the volume emission rate varies bi-cubically and use bi-cubic splines to discretize the integrals; this approach results in a smoother solution for the volume emission rate field. The following system of equations is solved using the VERT approach:

$$I_{1356} = 10^{-6} \sum \varepsilon\big(s(z, \phi)\big) T(|\tau(s_i) - \tau(s = 0)|, |t(s_i) - t(s = 0)|)\Delta s_i \tag{4}$$

F18 ALTAIR Over-flights			F19 ALTAIR Over-flights		
Date	UT (Hr: Min)	LT (Hr)	Date	UT (Hr: Min)	LT (Hr)
April 6	08:40	19.9	August 19	07:13	18.4
July 16	08:46	20.0	August 27	07:09	18.3
July 17	08:34	20.0	September 3	07:04	18.2
July 24	08:53	19.9	September 11	07:13	18.4
July 25	08:41	19.9	September 19	07:08	18.3
August 1	08:58	20.0	September 27	07:04	18.2
August 2	08:46	19.9	October 12	07:08	18.3
August 11	08:40	19.9	October 27	07:12	18.4
August 19	08:45	20.0			
August 26	09:02	20.0			
August 27	08:50	20.0			

Table 1: The dates and times of the SSULI flights over ALTAIR are shown. The F18 observations were made in 2010 while the F19 observations were made in 2014. LT indicates the local time in decimal hours and UT is the Universal Time.

where s is the path-length from the observer to voxel i, z is the altitude of the voxel, ϕ is the latitude of the voxel, and Δs_i is the path-length through the voxel (or the differential path length along the line-of-sight when the spline approach is used).

VERT Technique

Equation 4 is solved using the VERT technique a fast, non-negative iteration based on the Richardson-Lucy algorithm [*Richardson*, 1972; *Lucy*, 1974; *Dymond, Budzien, and Hei*, 2015, 2017]. The Richardson-Lucy algorithm seeks log-likelihood solution based on Poisson statistics, which is necessary as the SSULI measurements are based on photon counting and therefore contain photon shot or Poisson noise. The VERT approach uses a physicality constraint applied between iterations to smooth or regularize the solution. We regularize to the isotropic diffusion equation between steps [*Dymond, Budzien, and Hei*, 2015, 2017] and have found this method outperforms Maximum A Posteriori (MAP) and Tikhonov regularization approaches with very rapid convergence. The VERT approach was validated in previous work using SSULI measurements at 91.1 nm and ALTAIR electron densities [*Dymond et al.*, 2015, 2017a].

Inversion Approach

Once we have a set of SSULI measurements, we use the VERT technique to solve equation 4 to produce the 2D distribution of photon emission in a latitude/altitude plane that crosses the orbit plane at the equator. We account for radiation transfer due to resonant scattering and pure absorption in the path-length matrices used in VERT inversions. NRLMSISE-00 model was used to estimate the O and O_2 densities used in the radiation transfer and radiation transport calculations. After the VERT inversions are performed, we have the volume emission rate including radiation transport, ε. We solve equation 2 (inverse CFR Radiation Transport) to remove the resonant scattering contribution to the volume emission rate and infer the initial volume emission rate, ε_0. Then equation 1 is solved using Newton-Raphson iteration [*Press et al.*, 1992] to determine the electron density, which is compared to the ALTAIR results.
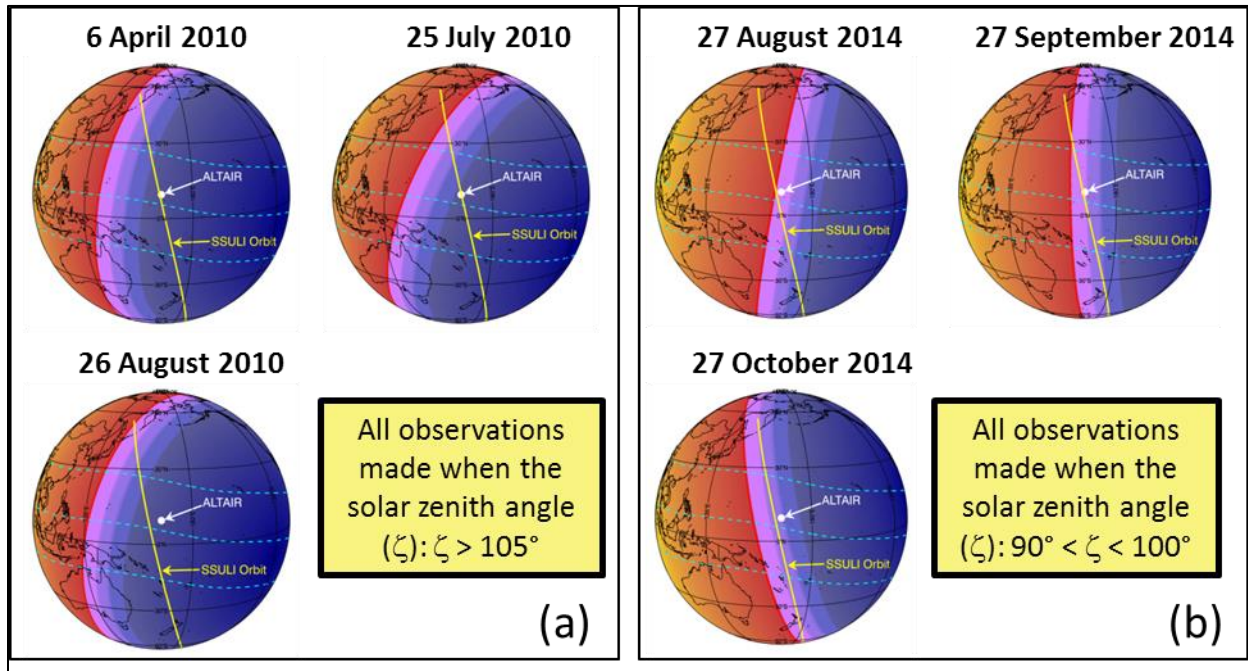
Figure 2: Panel (a) shows a sampling of the SSULI DMSP-F18 observations made in 2010. The yellow lines indicate the SSULI orbit with the ALTAIR location indicated by a white dot. The dashed blue lines indicate the magnetic equator and magnetic latitudes of ±20° in Apex coordinates [*Richmond*, 1995]. The solar zenith angle is indicated by pseudo-color with the yellows and reds (to the left sides of the images) indicating daytime and the blues and purples indicating nighttime (on the right sides of the images). The red arcs across the images indicate the solar terminator at a solar zenith angle of 90°. The colored bands to the right of the terminator are solar zenith angle bands of 90-95°, 95-100°, and 100-105°. Panel (b) shows a sampling of the SSULI DMSP-F19 observations made in 2014. The SSULI orbit planes are closer to the terminator with the 24 August 2014 terminator passing over ALTAIR at the time of the SSULI overflight. The F19 observations on 19 August, 27 August, and 3 September all are made close to the terminator.

4.   Validation Results

ALTAIR Measurements

Incoherent scatter radar maps were made along the orbit plane of the DMSP F18 and F19 spacecraft on several occasions during spring and summer of 2010 (F18) and late summer and fall of 2014 (F19) as shown in Table 1. The ALTAIR radar electron density measurements were made during DMSP passes which were nearly overhead the radar at Roi-Namur (9°23′46″ N, 167°28′33″ E) on the northern portion Kwajalein Atoll, Marshall Is. The radar scanned along the satellite trajectory for approximately 11 min using 1 s integration and ~1 km range gates. The subsequent electron density data were re-binned to a regular grid of 1° latitude and 5 km altitude resolution, this provided observations of the ionospheric electron density profiles which were within 0.5° of latitude, 2° of longitude and 10 minutes of the SSULI forward-looking limb scan observations. This is illustrated Figure 2, which shows the location of the DMSP satellite orbit track with respect to the radar and also indicates the solar illumination. An important consideration for this validation effort is that the SSULI measurements are made at ~0800/2000 local time during the F18 observations in 2010 and ~0620/1820 during the F19 observations in 2014. The DMSP-F18 observations are made at nighttime and are used to test and validate our approach under ideal conditions. The first 3 DMSP-F19 observations are made when the terminator is nearly overhead of ALTAIR with illumination gradients that are stressing to the technique but which allow us to evaluate the technique and radiation transport effects under non-ideal conditions. The remaining DMSP-F19 observations were made when the terminator was less than 10° from ALTAIR, but the SSULI lines-of-sight are more parallel to the terminator and, as a result, the illumination gradients are less severe.
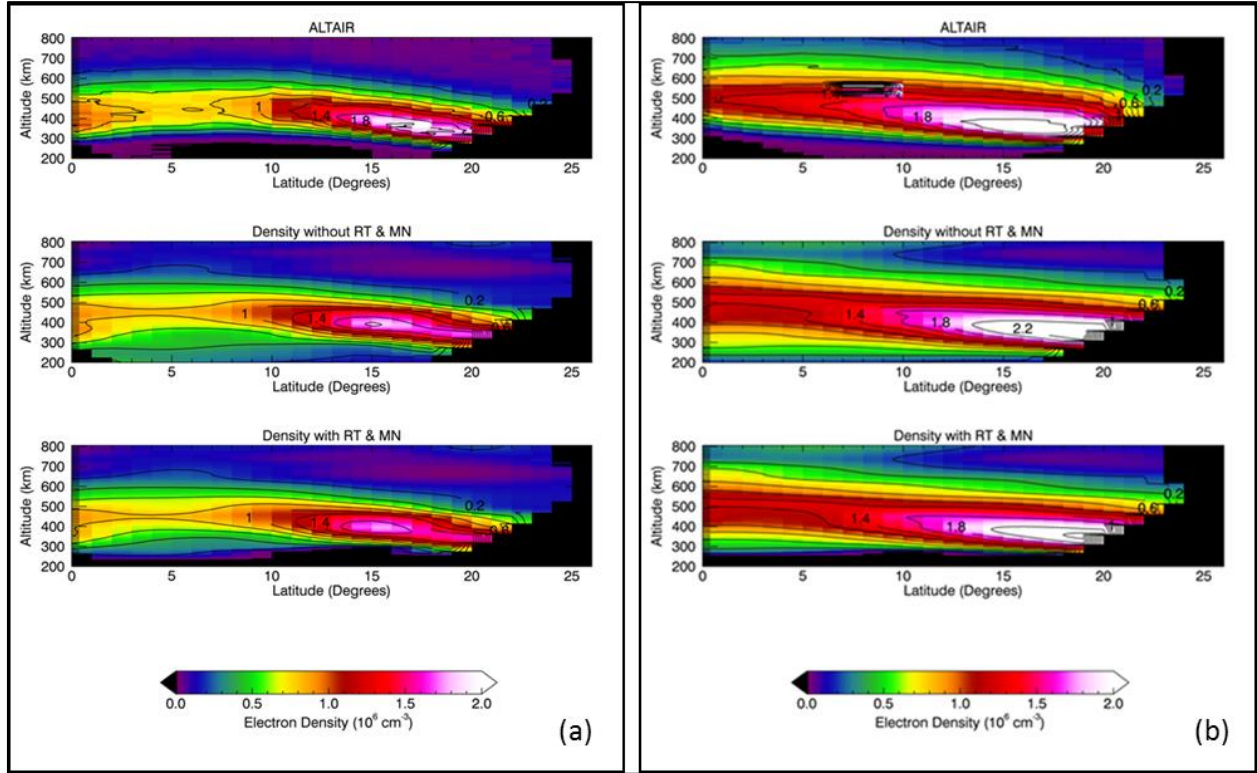
Figure 3: Typical SSULI retrievals are shown with the electron density color encoded, in units of 10^6 electrons/cm^3, with iso-contours of electron density over-plotted. Panel (a) shows the DMSP-F18 retrieval for the observations on 6 April 2010. The top image shows the ALTAIR measurements; the middle panel shows the SSULI retrieval ignoring radiation transport, transfer, and mutual neutralization; and the bottom panel shows the SSULI retrieval including radiation transport, transfer, and mutual neutralization. The mean error between the ALTAIR and SSULI measurements is 27%, ignoring radiation transport, transfer, and mutual neutralization, and 15%, when radiation transport, transfer, and mutual neutralization are included. Panel (b) shows the DMSP-F19 retrieval for the observations on 27 September 2014. The mean error between the ALTAIR and SSULI measurements is 7%, ignoring radiation transport, transfer, and mutual neutralization, and 1%, when radiation transport, transfer, and mutual neutralization are included. The ALTAIR measurements in the top image of panel (b) show a measurement artifact between 6°–10° latitude and 500–600 km altitude; this region containing this artifact was removed from the SSULI and ALTAIR data to make the percentage difference comparison.

SSULI Measurements and Comparison

Figure 3 shows typical SSULI retrievals are shown with the electron density color encoded, in units of 10^6 electrons-cm^{-3}. Panel (a) shows the DMSP-F18 retrieval for the observations on 6 April 2010. In the figure, the top images shows the ALTAIR measurements; the middle images show the SSULI retrievals ignoring radiation transport, transfer, and mutual neutralization; and the bottom images show the SSULI retrieval including radiation transport, transfer, and mutual neutralization. During the SSULI-F18 observations, the mean error between the ALTAIR and SSULI measurements was 27%, ignoring radiation transport, transfer, and mutual neutralization, and 15%, when radiation transport, transfer, and mutual neutralization were included. Panel (b) shows the DMSP-F19 retrieval for the observations on 27 September 2014. The mean error between the ALTAIR and SSULI measurements is 7%, ignoring radiation transport, transfer, and mutual neutralization, and -1%, when radiation transport, transfer, and mutual neutralization are included. A time series of SSULI-F18 retrievals is shown in Figure 4. The agreement between the SSULI and ALTAIR results is qualitatively good over the whole time period studied. Note that the peak density on 25 July 2010 was ~8×10^5 electrons-cm^{-3}; a density of this magnitude produces a brightness ~100 Rayleighs (R) on the limb. The sensitivity of the SSULI instrument was ~0.2 ct-s^{-1}-R^{-1} at 135.6 nm, resulting in a photon shot noise limited signal-to-noise ratio of ~0.22 during a 1 s exposure. Figure 5shows a time series of F19 retrievals with the first retrieval shown
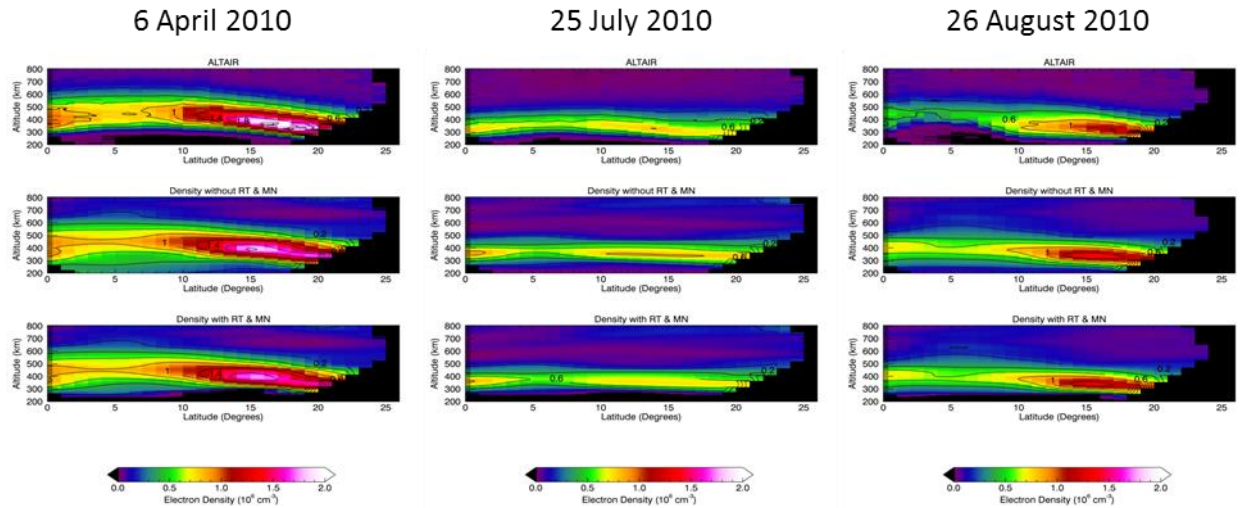
Figure 4: A time series of SSULI-F18 retrievals is shown. The agreement between the SSULI and ALTAIR results is good, in a qualitative sense. The layout of this figure is the same as in Figure 3.
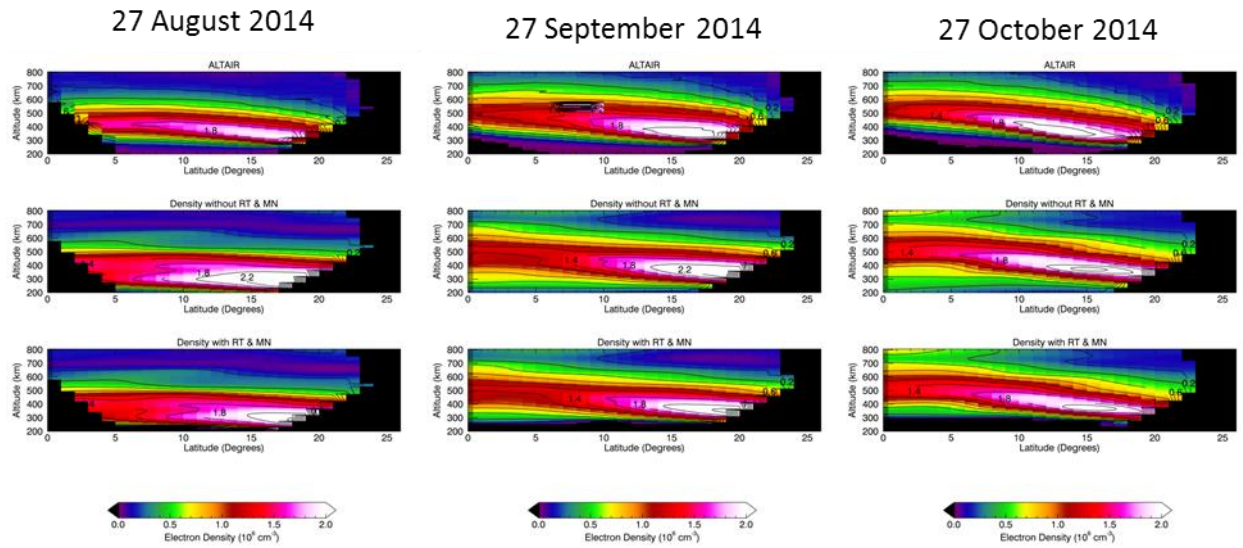

Figure 5: A time series of SSULI-F19 retrievals is shown. The agreement between the SSULI and ALTAIR results is qualitatively good, with the poorest agreement on 27 August 2014 when the terminator was over ALTAIR. The bottomside of the SSULI images is in poor agreement with the ALTAIR measurements due to a non-modeled contribution to the 135.6 nm emission caused by photoelectron impact excited atomic oxygen. The layout of this figure is the same as in Figure 3. The peak densities are significantly higher than they were during 2010 because in 2014 the measurements were made near solar maximum.

on 27 August 2014 in poor agreement with the ALTAIR measurements. The bottomside of the SSULI images on this day is in poor agreement with the ALTAIR measurements due to a non-modeled contribution to the 135.6 nm emission caused by photoelectron impact excited atomic oxygen. The peak densities are significantly higher than they were during 2010 because in 2014 the measurements were made near solar maximum.

The mean fractional differences between the SSULI and ALTAIR measurements with and without radiation transport, radiation transfer, and mutual neutralization are shown in Table 2. During the F18 observations made in 2010, the overall percentage difference was 20.3% when the effects were ignored and 6.5% when they were included. Including radiation transport, radiation transfer, and mutual neutralization produces more accurate retrievals in all cases with two exceptions on 1 August 2010 and 10

SSULI F18				SSULI F19		
Date	**Mean Fractional Difference**			**Date**	**Mean Fractional Difference**	
	No RT & MN	With RT & MN			No RT & MN	With RT & MN
2010-04-06	0.272	0.148		2014-08-19	0.731	0.595
2010-07-16	0.232	0.111		2014-08-27	0.332	0.220
2010-07-17	0.197	0.085		2014-09-04	0.382	0.278
2010-07-24	0.063	-0.045		2014-09-11	0.141	0.067
2010-07-25	0.070	-0.045		2014-09-19	0.283	0.169
2010-08-01	0.079	-0.095		2014-09-27	0.068	-0.011
2010-08-02	0.160	0.023		2014-10-12	-0.006	-0.108
2010-08-11	0.251	0.090		2010-10-27	0.224	0.142
2010-08-19	0.115	-0.051		Overall	0.233	0.052
2010-08-26	0.433	0.320				
2010-08-27	0.362	0.170				
Overall	0.203	0.065				

(Nighttime rows in F19: 2014-09-11 through 2010-10-27)

- **Mean fractional differences are shown**
- **Retrievals including Radiation Transport and Mutual Neutralization generally perform better**

Table 2: The mean fractional difference between the SSULI and ALTAIR measurements with and without radiation transport, radiation transfer, and mutual neutralization is shown. The overall percentage difference is 20.3% when the effects are ignored and 6.5% when they are included for the 2010 observations. For the F19 observations, the overall percentage difference was 23.3%, without radiation transport, radiation transfer, and mutual neutralization, and 5.2%, when those effects were included. Including radiation transport, radiation transfer, and mutual neutralization produces more accurate retrievals in all cases with two exceptions one on 1 August 2010 and the other on 12 October 2014, where the retrieval was more accurate when radiation transport, radiation transfer, and mutual neutralization were ignored.

October 2014, where ignoring the radiation transport, radiation transfer, and mutual neutralization performed slightly better. For the F19 observations made in 2014, the first three retrievals when the terminator was nearly overhead of ALTAIR produced the poorest agreement. This was expected as the algorithm did not include photoelectron impact excited emission, which was present on those days. Although the inclusion of radiation transport, radiation transfer, and mutual neutralization improved the retrieval accuracy compared to ignoring those effects. When we consider the nighttime observations made during the F19 observations made in 2014, the overall percentage difference between SSULI and ALTAIR was 23.3% when the effects of radiation transport, radiation transfer, and mutual neutralization were ignored and 5.2% when they were included. The overall improvement in the retrieval accuracy is ~14-18% when the effects of radiation transport, radiation transfer, and mutual neutralization are included in the inversions of the SSULI 135.6 nm measurements, which is consistent with the analysis of *Qin et al*. [2015].

We note that the accuracy of the SSULI 135.6 nm might be further improved by correcting for the electron temperature. In a previous study, *Dymond et al*. [2001b] validated 91.1 nm electron density profiles against ionosonde measurements and found that the inferred peak densities could be improved through the use of the International Reference Ionosphere [*Bilitza and Reinisch*, 2008] to estimate the electron temperature. The radiative recombination rate coefficient varies inversely as the square-root of the electron temperature, $T_e^{-0.5}$. The recombination rate coefficient used in the calculations in this work is for a temperature of 1160 K. In a previous study validating the 91.1 nm tomographic inversions against ALTAIR [*Dymond et al*., 2017a]

5.   Summary and Conclusions

We used coincident SSULI and ALTAIR measurements to attempt to answer several questions: 1) *How important is the modeling of the Mutual Neutralization source when calculating the electron densities in practical cases?* We demonstrated that inclusion of this source is important for the highest retrieval accuracy, although neglect of this source impacted our retrievals by ~15%. 2) *How important is the inclusion of radiation transport in practical cases?* Inclusion of radiation transport is important to accurately infer the bottomside electron density. However, the effect of the photons entrapped by multiple resonant scattering is partially mitigated by optical extinction effects. 3) *If proper modeling of these two sources of emission is included, is it possible to interpret 135.6 nm emission measurements in the region of the solar terminator?* We demonstrated that the retrievals are most accurate when all known effects impacting the photophysics of the 135.6 nm emission are included in the inversion algorithm; this is especially true in the terminator region. 4) *Lastly, is 2D radiation transport required in the terminator region?* Our results could not definitively answer this question due to measurement uncertainties. However, the O density gradients in the lower thermosphere where the photon entrapment occurs are stronger in the vertical direction than they are in the horizontal direction and, thus, the plane parallel (1D) approximation for the photon transport is adequate.

References

Bilitza, D., and B. W. Reinisch (2008), International Reference Ionosphere 2007: Improvements and new parameters, *Adv. Space Res.*, **42**, 599–609, doi:10.1016/j.asr.2007.07.048.

Dymond, K. F. (2009), Remote sensing of nighttime F region peak height and peak density using ultraviolet line ratios, Radio Sci., 44, RS0A28, doi:10.1029/2008RS004091.

Dymond, K. F., et al. (1997), An optical remote sensing technique for determining nighttime *F* region electron density, Radio Sci., 32(5), 1985–1996, doi:10.1029/97RS01887.

Dymond, K. F., et al. (2001a), Electron Densities Determined by the HIRAAS Experiment and Comparisons With Ionosonde Measurements, Geophys. Res. Lett., Vol. 28, No. 5, 927-930.

Dymond, K. F., et al (2001b), Electron Densities Determined By Inversion Of Ultraviolet Limb Profiles, J. Geophys. Res., Vol. **102**, No. A12, 30315-30323.

Dymond, K. F., and R. J. Thomas (2001), An algorithm for inferring the two-dimensional structure of the nighttime ionosphere from radiative recombination measurements, Radio Sci., 36(5), 1241–1254, doi:10.1029/2000RS002429.

Dymond, K. F., S. A. Budzien, and M. Hei (2015), Applications of Image Space Reconstruction Algorithms to Ionospheric Tomography, Proceedings of the 14th International Ionospheric Effects Symposium (IES2015), Paper #05A1, <http://ies2015.bc.edu/wp-content/uploads/2015/08/IES2015-Proceedings.pdf>, (11 Nov. 2015).

Dymond, K. F., et al. (2015), Validation of Special Sensor Ultraviolet Limb Imager (SSULI) Ionospheric Tomography using ALTAIR Incoherent Scatter Radar Measurements, Proceedings of the 14th International Ionospheric Effects Symposium (IES2015), Paper #05A3, <http://ies2015.bc.edu/wp-content/uploads/2015/08/IES2015-Proceedings.pdf>, (11 Nov. 2015).

Dymond, K. F., S. A. Budzien, and M. A. Hei (2017), Ionospheric-thermospheric UV tomography: 1. Image space reconstruction algorithms, Radio Sci., 52, 338–356, doi:10.1002/2015RS005869.

Dymond, K. F., et al. (2017a), Ionospheric-thermospheric UV tomography: 2. Comparison with incoherent scatter radar measurements, Radio Sci., 52, 357–366, doi:10.1002/2015RS005873.

Dymond, K. F., et al. (2017b), The Special Sensor Ultraviolet Limb Imager instruments, J. Geophys. Res. Space Physics, 122, doi:10.1002/2016JA022763.

Hedin, A. E. (1987), MSIS-86 Thermospheric Model, J. Geophys. Res., 92, 4649.

Lucy, L. B. (1974), An iterative technique for the rectification of observed distributions, Astron. J., Vol 79, No. 6, 745-754.

McCoy, R. P., K. F. Dymond, G. G. Fritz, S. E. Thonnard, R. R. Meier, and P. A. Regeon (1994), Special Sensor Ultraviolet Limb Imager (SSULI) - an Ionospheric and Neutral Density Profiler for DMSP Satellites, Opt. Eng., Vol. 33, #2.

Meier, R. R. (1991), Ultraviolet Spectroscopy and Remote Sensing of the Upper Atmosphere, Space Sci. Rev., 58, 1-186.

Meléndez-Alvira, et al. (1999), Analysis of the oxygen nightglow measured by the Hopkins Ultraviolet Telescope: Implications for ionospheric partial radiative recombination rate coefficients, J. Geophys. Res., 104(A7), 14901–14913, doi:10.1029/1999JA900136.

Picone, J. M., et al. (2002), NRLMSISE-00 empirical model of the atmosphere: Statistical comparisons and scientific issues, J. Geophys. Res., 107(A12), 1468, doi:10.1029/2002JA009430.

Press, W. H., et al. (1992), Numerical Recipes: The Art of Scientific Computing, Cambridge University Press, New York, NY.

Qin, J., et al. (2015), Radiative transfer modeling of the OI 135.6 nm emission in the nighttime ionosphere, *J. Geophys. Res. Space Physics*, 120, 10116–10135, doi:10.1002/2015JA021687.

Richardson, W. H. (1972), Bayesian-based iterative method of image restoration, J. Opt. Soc. Amer., Vol. 62, No. 1, 55-59.

Richmond, A. D. (1995), Ionospheric electrodynamics using magnetic apex coordinates, J. Geomag. Geoelectr., 47, 191.

Straus, P. R. (and the UV Sensor Cal/Val Team inc. K. F. Dymond) (2012), Calibration/Validation Final Report for the Special Sensor Ultraviolet Limb Imager (SSULI) and the Special Sensor Ultraviolet Spectrographic Imager (SSUSI) on the Defense Meteorological Satellite Program (DMSP) F18 Spacecraft, Aerospace Technical Report, Aerospace Corp., TOR-2012(1550)-5.

Tsunoda, R. T., et al. (1979), Altair: an incoherent scatter radar for equatorial spread F studies, Radio Sci., 14(6), 1111–1119, doi:10.1029/RS014i006p01111.

Wang, J., et al. (1987), Effects of the Close Approach of Potential Curves in Photoabsorption by Diatomic Molecules—II. Temperature Dependence of the O_2 Cross Section in the Region 130–160 nm, J. Quant. Spectroscopy and Radiative Transfer, 38, 19.